Accepted Manuscript

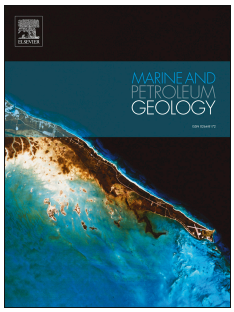

Permeability in Rotliegend Gas Sandstones to gas and brine as predicted from NMR, mercury injection and image analysis

Esther Rosenbrand, Ida Lykke Fabricius, Quentin Fisher, Carlos Grattoni

PII: S0264-8172(15)00034-3

DOI: 10.1016/j.marpetgeo.2015.02.009

Reference: JMPG 2134

To appear in: *Marine and Petroleum Geology*

Received Date: 30 April 2014

Revised Date: 14 January 2015

Accepted Date: 8 February 2015

Please cite this article as: Rosenbrand, E., Fabricius, I.L., Fisher, Q., Grattoni, C., Permeability in Rotliegend Gas Sandstones to gas and brine as predicted from NMR, mercury injection and image analysis, *Marine and Petroleum Geology* (2015), doi: 10.1016/j.marpetgeo.2015.02.009.

Permeability in Rotliegend Gas Sandstones to gas and brine as predicted from NMR, mercury injection and image analysis

Esther Rosenbrand[1], Ida Lykke Fabricius[1], Quentin Fisher[2], Carlos Grattoni[2]

1 – Department of Civil Engineering, Technical University of Denmark, Brovej 118, 2800 Kgs, Lyngby, Denmark

2 – School of Earth and Environment, University of Leeds, Leeds, LS2 9JT, UK

Addresses:

Postal: Esther Rosenbrand, Technical University of Denmark, Brovej building 118, 2800 Kongens Lyngby, Denmark.

Email: esro@byg.dtu.dk

Phone: +45 45 25 14 16

Postal: Ida Lykke Fabricius, Technical University of Denmark, Building 119 Brovej 118, 2800 Kongens Lyngby, Denmark.

Email: ilfa@byg.dtu.dk

Phone: +45 45252162

Postal: Quentin Fisher, room 7.134, School of Earth and Environment, Maths/Earth and Environment Building, The University of Leeds, Leeds LS 9JT, United Kingdom.

Email: q.j.fisher@leeds.ac.uk

Phone: +44(0) 113 34 31920

Postal: Carlos Grattoni, room 7.126, School of Earth and Environment, Maths/Earth and Environment Building, The University of Leeds, Leeds LS 9JT, United Kingdom.

Email: C.A.Grattoni@leeds.ac.uk

Phone: +44(0) 113 34 35214 / 30474

Permeability characterisation of low permeability, clay-rich gas sandstones is part of production forecasting and reservoir management. The physically based Kozeny (1927) equation linking permeability with porosity and pore size is derived for a porous medium with a homogeneous pore size, whereas the pore sizes in tight sandstones can range from nm to μm. Nuclear magnetic resonance (NMR) transverse relaxation was used to estimate a pore size distribution for 63 samples of Rotliegend sandstone. The surface relaxation parameter required to relate NMR to pore size is estimated by combination of NMR and mercury injection data. To estimate which pores control permeability to gas, gas permeability was calculated for each pore size increment by using the Kozeny equation. Permeability to brine is modelled by assuming a bound water layer on the mineral pore interface. The measured brine permeabilities are lower than predicted based on bound water alone for these illite rich samples. Based on the fibrous textures of illite as visible in electron microscopy we speculate that these may contribute to a lower brine permeability.

Keywords: permeability; tight sandstone; bound water; image analysis; NMR

Nomenclature

b = slip factor, t^2L/m, 1/Pa

c_0 = pore shape parameter, -

c = parameter relating porosity to permeability and specific surface area, -

$f_{NMR,i}$ = fraction of pore volume corresponding to i^{th} T_2 time $T_{2,i}$, -

$f_{Hg,i}$ = fraction of pore volume corresponding to i^{th} capillary pressure increment for mercury injection, -

$f_{\phi_{eff}}$ = fraction of pore volume that controls permeability, -

$fw_{nmr,i}$ = fraction of mobile pore water corresponding to i^{th} $T_{2,i}$ time, -

k = absolute permeability, L^2, m^2, mD

k_a = apparent permeability to gas flow, L^2, m^2, mD

k_w = brine permeability, L^2, m^2, mD

M = molar mass, m/n, g/mol

P_c = capillary pressure, m/t^2L, Pa

r = pore radius, L, m

r_{eff} = effective pore radius for pores that control permeability $r_{eff} = 2/S_{p,eff}$, L, m

$r_{max,gas}$ = maximum pore radius that controls permeability to gas, L, m

$r_{max,brine}$ = maximum pore radius that controls permeability to brine, L, m

R_g = gas constant, $L^2m/(s^2Tn)$, J/mol K

S = specific surface area per bulk volume, L^{-1}, m^2/cm^3

S_p = specific surface area per pore volume, L^{-1}, m^2/cm^3

$S_{p,i}$ = specific surface area per pore volume for pores with T_{2i}, L^{-1}, m^2/cm^3

$S_{p,eff}$ = specific surface area per pore volume for pores that control permeability, L^{-1}, m^2/cm^3

$Sw_{P,i}$ = specific surface area per pore volume for mobile water, L^{-1}, m^2/cm^3

T = temperature, T, K

$T_{2,i} = i^{th}$ T_2 time, t, s

$T_{2,i_{max}}$ = cut-off T_2 time, t, s

$T_{2,Gmean}$ = geometric mean T_2 time, t, s

V = bulk volume of sample, L^3, m^3

V_{Hg}= volume of mercury injected, L^3, m^3

γ = surface tension, m/t^2, N/m

θ= contact angle, °

λ = mean free path length gas, L, m

μ = viscosity, m/tL, Pa.s

ρ = surface relaxivity, L/t, m/s

τ = thickness of immobile water, L, m

Γ = tortuosity, -

ϕ = porosity, -

ϕ_{eff} = porosity that controls permeability, $\phi f_{\phi_{eff}}$, -

1. Introduction

The Permian Rotliegend sandstones remain a significant source of gas within Europe. Historically, production has been primarily from reservoirs with moderate to high permeability, 10 mD-1D, in fields such as the Groningen gas field in the north of the Netherlands, which has a high productivity. For future supply, exploration targets gas sandstone reservoirs that have less favourable properties (Gaupp and Okkerman, 2011).

Porosity and permeability may be reduced by quartz cementation in sandstones with a low clay content. The percolation threshold is a minimum porosity below which intergranular pores no longer form a connected flow path (Hunt 2009). For rocks with a porosity close to the percolation threshold larger intergranular pores may only be connected through thin fractures, microcracks; therefore thin microcracks, and not larger intergranular pores, would control the permeability (Brower and Morrow, 1985; Mavko and Nur, 1997; Ostensen, 1983). Larger intergranular pores may also not form a connected flow path in clay-rich sandstones with a higher porosity. When clay minerals occlude the intergranular pore space, this may disconnect larger pores (Desbois et al. 2011). In such sandstones, micropores among clay minerals would control permeability.

Permeability as measured using brine is often lower than permeability as measured using gas (Heid et al., 1950; Jones and Owens, 1980). Gas slip may contribute to a higher gas permeability, and this effect is larger in samples with a small equivalent pore size (Klinkenberg, 1941). Bound water may reduce the mobile fluid volume for brine flow as compared to gas flow (Andreassen and Fabricius, 2010; Byerlee, 1990; Heid et al., 1950; Luffel et al., 1993; Solymar et al., 2003). An immobile water layer would have a greater effect in smaller pores. Therefore the size of the pores that control permeability is relevant to the difference between permeability to brine and to gas.

Clay minerals may also affect permeability to brine by other mechanisms. Delicate clay minerals, such as thin illite clay fibres that grow perpendicular to the grain surface, may collapse onto the grain surface during drying (Luffel et al. 1993; de Waal et al. 1988). This effect is found to be partially reversible when samples are saturated again (Luffel et al., 1993). Mobilisation of clay particles may occur when clay minerals and

quartz grains have a similar sign surface charge. Dissolved ions shield the surface charge by forming an electrical double layer (EDL) (Lyklema 1995). In low salinity brine, there is less shielding, resulting in a high EDL repulsion between surfaces that could mobilise particles and reduce permeability (Khilar and Fogler, 1984).

In this study we investigate permeability of 63 Rotliegend sandstones to gas and to brine; samples contain over 6 wt.% clay minerals, which allows for an investigation of textural effects on permeability. Mineralogy was quantified using X-ray diffraction (XRD) (Hillier, 1999, 2000). Backscatter electron microscopy (BSEM) images were analysed to characterise clay morphology and to quantify clay-free porosity to estimate percolation effects. Pore size distributions were measured using mercury (Hg) injection porosimetry and low field nuclear magnetic resonance (NMR). The surface relaxivity, which is needed to convert NMR to equivalent pore size, is estimated by comparing Hg injection data to NMR. Gas permeability was modelled from the pore size distribution from NMR as in Hossain et al (2011). The fraction of the pores that control permeability was estimated by comparison of measured and modelled permeability. Brine permeability was modelled by reducing the porosity to brine by an immobilised layer on the mineral-fluid interface, but in several cases an unrealistically thick immobile water layer was predicted. This indicates that bound water is not the only cause of the lower brine permeability, which might also be due to the presence of fibrous illite.

1.2 Geological setting

The Rotliegend sandstones were deposited in the South Permian Basin (SPB), which is bounded by the Mid-North Sea High and the Ringkøbing-Fyn High in the north and by the London-Brabant Massif and the Rhenish High in the South. In an East-West direction, the SPB ranges from the eastern UK to central Europe (Gaupp and Okkerman, 2011).

Diagenetic processes in the Rotliegend sandstones were studied by several authors and Gaupp and Okkerman (2011) review how these processes affect reservoir quality. Authigenic minerals that are abundant throughout the SPB include quartz, carbonates, iron oxides, illite, chlorite and kaolin (Gaupp and Okkerman, 2011). The

red colour of many samples is due to the presence of hematite (an iron oxide) (Torrent and Schwertmann, 1987). The sandstones are sometimes grey due to bleaching during diagenesis (Gaupp and Okkerman, 2011); however hematite may still be present in the form of small grains between clay particles (Desbois et al., 2011). Regional diagenetic processes were affected by the chemistry of ground waters, uplift, temperature history, and later fluid flow, resulting in variations in the clay mineral distribution (Gaupp and Okkerman, 2011).

1.3 Pore space from NMR and Hg injection

The pore size, or $\boldsymbol{S_p}$, distribution can be obtained from NMR (Coates et al. 1999). In NMR, hydrogen nuclei in water saturated samples are aligned in a permanent magnetic field and flipped in a temporary magnetic field. The consequent rate of decay of magnetisation is measured and converted to a transverse relaxation time, $\boldsymbol{T_2}$ (Coates et al., 1999). The decay rate of magnetisation is higher near the water-mineral interface than in the bulk water. So in the fast diffusion regime, in which the majority of hydrogen nuclei are relaxed at the water mineral interface by surface relaxation, the $\boldsymbol{T_2}$ time reflects $\boldsymbol{S_p}$ (Eq. 1)

$$S_p = \frac{1}{\rho T_2}$$

Eq. 1

where ρ is the surface relaxivity, which is a measure of the rate at which relaxation occurs at the surface. For samples with a range of pore sizes, NMR yields a T_2 distribution where the amplitude, $f_{NMR,i}$ is the fraction of the total porosity that corresponds to a given T_2, $T_{2,i}$, thus $\phi\, f_{NMR,i}$ is the pore volume that corresponds to $T_{2,i}$.

The surface relaxivity is required in order to estimate an S_p distribution from the T_2 distribution The surface relaxivity depends on the mineral-fluid interaction, and in particular on the presence of iron, which increases ρ (Keating and Knight, 2007, 2010; Matteson and Tomanic, 2000). Several authors combined NMR with Hg injection to estimate an effective ρ (Coates et al., 1999; Dastidar et al., 2006; Mbia et al., 2014).

In Hg injection the fraction of the porosity, $f_{Hg,i}$ which is injected for each successive capillary pressure increment, $P_{c,i}$, is measured. Capillary pressure can be related to pore radius, r, by the Washburn (1921) equation:

$$r = -\frac{2\gamma\cos(\theta)}{P_c}$$

Eq. 2

where P_c is the capillary pressure, γ is the surface tension and θ is the contact angle. For mercury injection $\gamma = 0.48$ N/m and $\theta = 140°$. Capillary pressure from Hg-injection can be integrated over the volume of mercury injected to obtain the specific surface, S, in Eq. 3 (Giesche, 2006; Rootare and Prenzlow, 1967).

$$S = -\frac{1}{V\gamma\cos(\theta)}\int P_c dV_{Hg}$$

Eq. 3

where V_{Hg} is the volume of mercury injected, and V is the sample bulk volume. For stepwise injection of mercury where $f_{Hg,i}$ is the fraction of the porosity that is filled by mercury for the pore pressure increment $P_{c,i}$, so that $\phi f_{Hg,i} = dV_{Hg,i}/V$, then S is given by Eq. 4.

$$S = -\frac{\phi}{\gamma\cos(\theta)}\sum P_{c,i} f_{Hg,i}$$

Eq. 4

The specific surface area in each T_2 increment from NMR is the product of the pore volume in the increment and the specific surface area per pore volume:

$$S_i = \phi f_{NMR,i} S_{p,i} = \frac{\phi f_{NMR,i}}{\rho T_{2,i}}$$

Eq. 5

The total specific surface area from NMR is given by summation of the surface area for each T_2 time over the pore volume. When ρ is assumed homogeneous, S is given by

$$S = \frac{\phi}{\rho} \sum \frac{f_{NMR,i}}{T_{2,i}}$$

Eq. 6

Where $f_{NMR,i}$ is the fraction of the porosity that corresponds to $T_{2,i}$. Assuming 100% mercury saturation, ρ is given by Eq. 7.

$$\rho = \frac{-\gamma \cos(\theta) \sum \frac{f_{NMR,i}}{T_{2,i}}}{\sum P_{c,i} f_{Hg,i}}$$

Eq. 7

1.4 Permeability modelling

Kozeny (1927) derived Eq. 8 to model permeability in porous media based on flow in capillaries with a uniform pore size.

$$k = \frac{c\phi}{S_p^2}$$

Eq. 8

where k is permeability, ϕ is porosity, c is a parameter that accounts for pore geometry ($c = {}^{1}/_{2}$ for straight cylindrical pores), and S_p is the specific surface area, S, per unit pore volume:

$$S_p = \frac{S}{\phi}$$

Eq. 9

S_p is inversely proportional to the equivalent pore radius, r. For a cylindrical pore:

$$r = \frac{2}{S_p}$$

Eq. 10

As flow does not follow a straight flow path, Carman (1937) modified the Kozeny Equation by expressing c as a function of tortuosity Γ and pore shape c_0, i.e., $c = c_0\Gamma$ ($c_0 = {}^{1}/_{2}$ and $\Gamma = 1$ for straight cylindrical pores). Forms of the Kozeny equation in which the parameter c reflects tortuosity are often referred to as Kozeny-Carman equations (e.g., Bear, 1972; Berryman and Blair, 1987; Mavko and Nur, 1997). A value of $c = 0.2$ was fit to experimental data of powders and crushed sand packs (Carman, 1937; Donaldson, 1975). Electrical resistivity or diffusion measurements are used to estimate Γ by some authors e.g., Berryman and Blair (1987), Cornell and Katz (1953), Dullien (1975), Pape et al. (2006), Walsh and Brace, (1984). However, tortuosity for hydraulic flow would not necessarily be the same as tortuosity for diffusion and electrical conduction (Bear, 1972; Carman, 1937; Pape et al., 2006). Whereas diffusion and electrical conduction in a pore have a piston-like displacement, fluid flow has a velocity profile with a lower velocity on the fluid-mineral interface.

Rather than considering a tortuous flow path, Mortensen et al. (1998) used a conceptual model of the rock where only a fraction of ϕ contributes to flow. Their c (cf. Eq. 11) reduces ϕ so that only porosity parallel to

the sample axis conducts flow (Mortensen et al., 1998). This equation is derived for straight cylindrical capillaries and accounts for the area in the intersections among capillaries.

$$c = \left(4\cos\left(\frac{1}{3}\arccos\left(\phi\frac{64}{\pi^3} - 1 \right) + \frac{4}{3}\pi \right) + 4 \right)^{-1}$$

Eq. 11

The value of c is 0.20 ± 0.02 for $2\% < \phi < 32\%$, which is similar to the empirical $c_0\Gamma$ by Carman (1937).

Kozeny's (1927) equation can be used to calculate the permeability from NMR by substitution of Eq. 1 into Eq. 8 (Hossain et al. 2011). The permeability k_i for the porosity $\phi f_{NMR,i}$ that corresponds to each $T_{2,i}$ interval is given by Eq. 12 (Hossain et al., 2011).

$$k_i = c_i \rho^2 \phi f_{NMR;i} T_{2,i}{}^2$$

Eq. 12

where c is estimated as a function of porosity (cf. Eq. 11) to avoid introducing a tortuosity parameter. Those authors sum the permeability of all pore size increments to predict the sample permeability, for sandstones with a clay-free porosity > 20%. This would suggest that the larger pores form a connected flow path in those samples. For sandstones where larger pores do not form a connected flow path, the permeability in the largest pore would not be expected to contribute to the sample permeability.

1.4.1 Permeability modelling: gas slip

Gas slip contributes to a higher apparent permeability to gas, due to a non-zero velocity on the pore fluid interface (Klinkenberg, 1941). The higher apparent permeability due to gas slip is related to the true permeability by Eq. 13 and Eq. 14(Klinkenberg. 1941).

$$k_a = k\left(1+\frac{b}{P}\right)$$

Eq. 13

$$b = \frac{4c\lambda P}{r}$$

Eq. 14

where λ is the mean free path length. Various authors use Eq. 15 by Loeb (1927) to estimate the mean free path length e.g., Florence et al. (2007), Civan (2010).

$$\lambda = \frac{\mu}{P}\sqrt{\frac{\pi R_g T}{2M}}$$

Eq. 15

where μ is the gas viscosity, P is the mean pore pressure, R_g is the gas constant, T is temperature and M is the molar mass of the gas. Therefore, when the size of the pores which control permeability is known, the effect of gas slip on the apparent permeability can be estimated.

1.4.2 Permeability modelling: immobile water

The effect of bound water can be modelled as a reduction of the effective pore size; therefore we model the effect of bound water on the pore size distribution from NMR. The free pore volume that is available to water, $\phi fw_{nmr,i}$, is given by the fraction that is available to air, $\phi f_{NMR,i}$, minus the thickness of bound water, τ, on the grain surface:

$$\phi fw_{NMR,i} = \phi f_{NMR,i} - \tau S_i$$

Eq. 16

Substitution of Eq. 1 where $S_p = S/\phi$ gives:

$$\phi fw_{NMR,i} = \phi f_{NMR,i} - \frac{\tau\phi}{\rho T_{2,i}}$$

Eq. 17

Whereas $\sum f_i = 1$, i.e. all porosity is available for gas flow, due to bound water $\sum f_{i,w} < 1$. As a first approximation, S is constant so that the specific surface per pore volume of mobile water, $Sw_{p,i}$ is obtained by substituting the porosity of mobile water, $\phi fw_{NMR,i}$, for the total porosity, $\phi f_{NMR,i}$, in Eq. 9 yielding:

$$Sw_{p,i} = \frac{S_i}{\phi fw_{NMR,i}} = \frac{S_i}{\phi f_{NMR,i}} \frac{f_{NMR,i}}{fw_{NMR,i}} = S_{p,i} \frac{f_{NMR,i}}{fw_{NMR,i}}$$

Eq. 18

Substitution into Eq. 12 yields the brine permeability, $k_{w,i}$, of pores for a given T_{2i} in Eq. 19, where $c_{w,i}$ is cf. Eq. 11 using $fw_{NMR,i}$.

$$k_{w,i} = \rho^2 c_{w,i} \phi fw_{NMR,i} T_{2,i}^2 \left(\frac{fw_{NMR,i}}{f_{NMR,i}} \right)^2$$

Eq. 19

2. Experimental methods

We studied 63 samples from six wells from sectors in the North Sea and from sectors in Poland. Samples have a current burial depth in the range of 2440-3961 m. Cylindrical plugs with ~3.8 cm diameter and 4-6 cm length were cut from reservoir cores. Plugs were cleaned using a Soxhlet extractor using a mixture of methanol and dichloromethane.

Polished thin sections for BSEM were produced from side trims. Polished thin sections and stubs of fractured samples were examined using a CAMSCAN CS44 high performance scanning electron microscope equipped with a secondary electron detector and a high resolution solid state four quadrant back scattered electron (BSE) detector. Representative images using BSE were taken for each sample and saved with 256 grey levels.

Mineralogy was quantified using XRD, using a spray technique as described in Hillier (1999, 2000) in order to produce samples without significant preferred orientations. The samples were dried in an oven at 60°C for 48 hours prior to measurements.

Porosity was measured using a helium gas expansion porosimeter. Gas permeability was measured by flow of helium gas parallel to the plug axis. Samples were subjected to in situ confining stress in order to close fractures that resulted from unloading, and at 6.7 MPa pore pressure in order to minimise the effect of gas slip. For samples with permeability below 0.1 mD, permeability was measured using a pulse-decay technique (Jones, 1997) using a modified Corelabs PDP 200 pulse decay permeameter that has been adapted so that measurements can be made at up to 70 MPa confining pressure. Permeability was calculated using the software for the PDP 200 supplied by Corelabs as in Jones (1997). Samples with a higher permeability were measured using steady state permeametry (API, 1998). Brine permeability was measured using 200,000 ppm NaCl solution to avoid particle mobilisation and full saturation was verified by using NMR.

Mercury (Hg) was injected into the evacuated core plugs by increasing the pressure stepwise up to 413.7 MPa (60 000 psi). Mercury measurements were performance corrected.

NMR T_2 relaxation time measurements were performed on brine saturated samples using a MARAN ULTRA from Oxford Instruments, which has a 51 mm probe and a 2 MHz operating frequency. The Carr-Purcel-Meiboom-Gill (CPMG) pulse sequence was used to generate the magnetization decay with an echo spacing of 0.1 ms, and repeat delay of 10 s between successive scans. The decaying magnetization was mapped to a T_2 distribution using the WinDXP programme software provided by Oxford Instruments. The signal amplitude was calibrated using standards with a known volume of doped water.

3. Image Analysis

Image analysis was performed on images with a pixel length of 3 μm using Matlab 2012b (The MathWorks). Pores between clay particles or microfractures can be smaller than the pixel size. Pixels that contain both clay minerals and porosity have a lower brightness than pixels that contain only minerals (Peters, 2009). Therefore a first threshold was used to segment the image in to the darker porosity and clay fraction and the lighter other minerals. A second lower threshold was used to segment clay-free porosity and the clay fraction, whereby the clay fraction consists of pixels containing both clay minerals and pores between clay particles. Thresholds were selected based on the histogram of pixel intensity (Figure 1). We did not equalise histograms for different samples as these have different shapes; e.g., some samples have a distinct peak of clay-free porosity and others do not. BSEM images with a pixel length of 0.6 μm, and SEM images were used in order to characterise clay morphology.

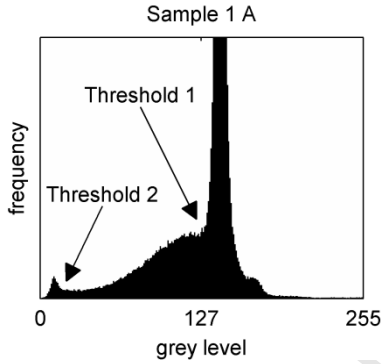

Figure 1: Histogram of pixel intensity for a backscatter electron microscopy image of sample 1A. Threshold 1 separates solid grains, with a higher intensity, from clay minerals and pore volume. Threshold 2 separates pixels that contain clay minerals and pore volume, with a higher intensity, from pore volume without clay minerals.

4. Results

4.1 Mineralogy

Samples are subarkoses or arkoses according to the classification of McBride (1963). Illite/mica is present in all samples, additionally some samples contain kaolin and other samples contain chlorite. Although distinction between chlorite and kaolin clay minerals based on XRD may be difficult for iron rich chlorite minerals (Grim, 1953), petrographical analysis did not indicate errors in the XRD analysis of these minerals. The sum of the clay mineral contents ranges from 6% to 16% of the solid mass.

The main variation among samples is due to differences in clay content. Accordingly, some authors have described regional variation in the clay mineralogy of Rotliegend sandstones in the Netherlands in terms of clay provinces (Gaupp and Okkerman, 2011). As the effect of clay minerals on the pore space is related to the morphology of the clays, i.e. the type of clay mineral and the abundance (Landrot et al. 2012; Wilson and Pittman, 1977; Wilson et al. 2014) samples were grouped based clay mineralogy. Groups 1 and 3 are kaolin bearing sandstones; kaolin is the dominant clay mineral in Group 1, whereas illite/mica is dominant in Group 3. Samples in groups 2 and 5 both contain grain lining chlorite and illite clay minerals; due to the relatively low clay content in these samples, clay minerals only account for a small fraction of the intergranular porosity in Group 5. Samples in Group 4 contain only illite/mica. The average mineralogy from XRD for the five groups of samples is shown in Table 1.

Table 1: Average mineral content for the five groups from XRD given as mass %. Standard deviation within groups is given in brackets.

	Gr. 1		Gr. 2		Gr. 3		Gr. 4		Gr. 5	
Quartz	72	(4)	78	(5)	75	(3)	79	(3)	76	(5)
Albite	0.6	(0.9)	4.3	(0.7)	1.6	(0.4)	2.7	(1.4)	4.4	(1.2)
Microcline	5.4	(0.3)	0.2	(0.4)	1.9	(1.4)	4.9	(0.7)	5.4	(1.3)
Calcite	0	(0)	0	(0)	0.06	(0.13)	0.04	(0.07)	0.07	(0.13)
Dolomite	6	(4)	4	(2)	6	(4)	5.5	(1.3)	3.6	(1.3)
Siderite	0.5	(0.5)	0.01	(0.03)	2	(2)	0	(0)	0.8	(0.7)
Illite/Mica	5	(1.0)	10	(2)	9	(3)	6.7	(1.1)	8	(2)
Kaolinite	10.8	(1.0)	0	(0)	3.4	(1.3)	0	(0)	0	(0)
Chlorite	0	(0)	6	(2)	0	(0)	0	(0)	2.2	(0.7)
Pyrite	0.4	(0.4)	0.1	(0.2)	0.3	(0.4)	0.01	(0.04)	0	(0)
Anhydrite	0.01	(0.02)	0.02	(0.03)	0.4	(0.8)	0.3	(0.9)	0	(0)
Barite	0	(0)	0	(0)	0.08	(0.2)	0	(0)	0	(0)
no samples	*9*		*11*		*14*		*22*		*7*	

4.2 Pore space

4.2.1 Image analysis

Figure 2 shows the BSEM images and the segmented BSEM images for two characteristic samples from each group. The A samples represent samples with a relatively low mean T_2, and samples B represent a higher mean T_2, Table 2 shows how many samples have a T_2 distribution that is similar to sample A and sample B for each group. The area fractions of clay minerals and all pores, and of only clay-free pores, are also shown in Table 2. The area of the clay fraction including all pores equals the sum of the He-porosity and the clay solid volume from XRD for all ten samples. This indicates that the interrogation area in image analysis was representative. Images at 0.6 μm/pixel resolution were acquired in order to characterise clay morphology, therefore no quantitative analysis was applied to these.

Microcracks along grain boundaries or through clay aggregates can be observed in BSEM images. These microcracks might be due to unloading as the thin sections are prepared at ambient stress. Permeability measurements were made at in situ stress to minimise the effect of flow through microcracks. Therefore the

BSEM images may not represent the connectivity of the sample during the permeability test; so that the segmented images in which microcracks are largely eliminated might better represent the pore space during the permeability tests.

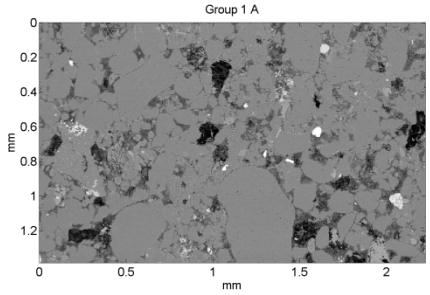

a

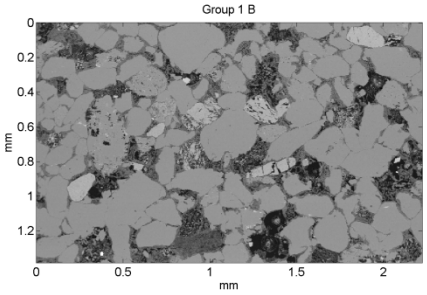

b

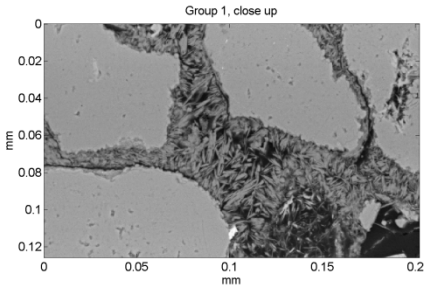

c

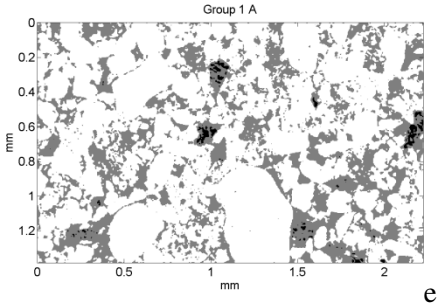

d

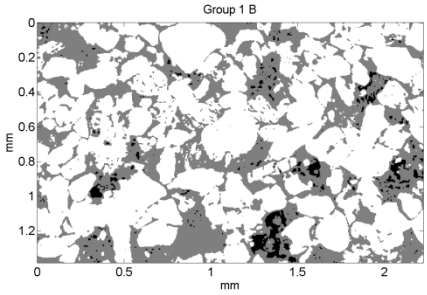

e

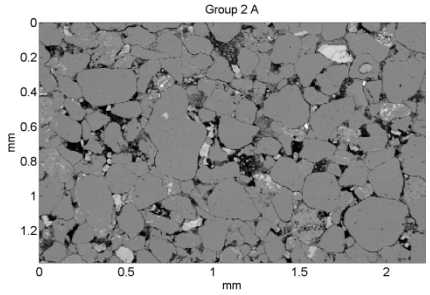

f

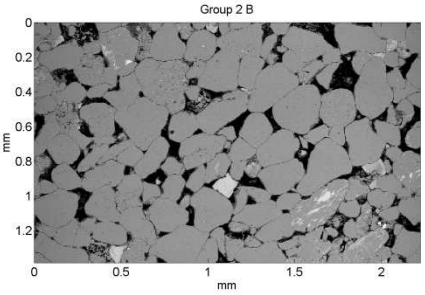

g

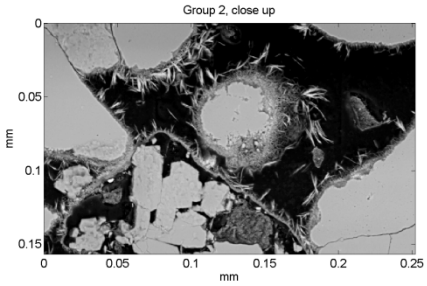

h

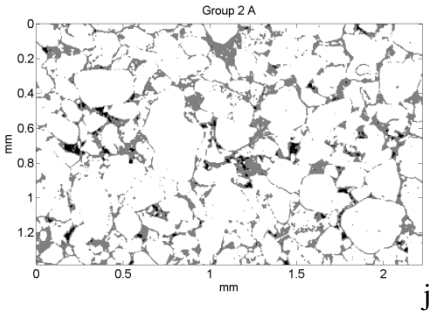
Group 2 A
mm
mm

i

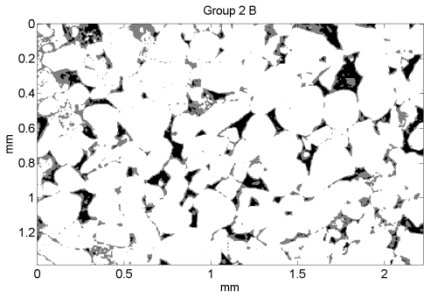
Group 2 B
mm
mm

j

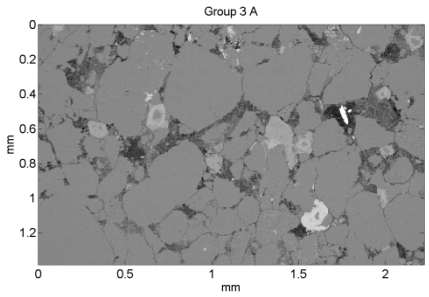
Group 3 A
mm
mm

k

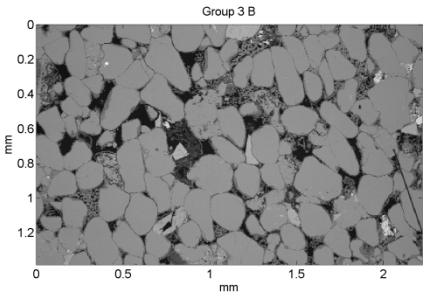
Group 3 B
mm
mm

l

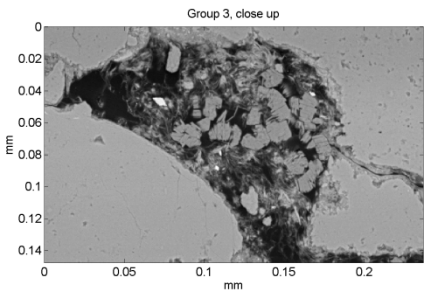
Group 3, close up
mm
mm

m

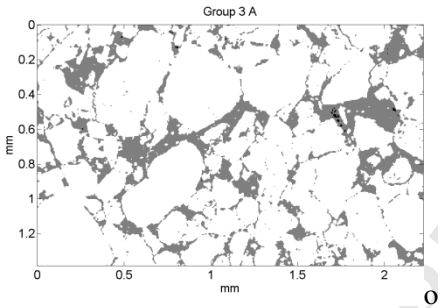
Group 3 A
mm
mm

n

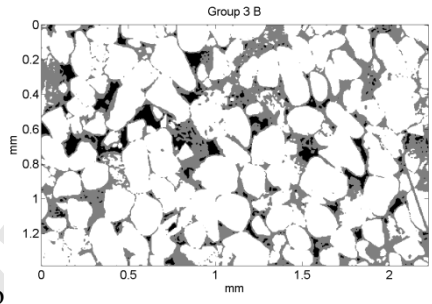
Group 3 B
mm
mm

o

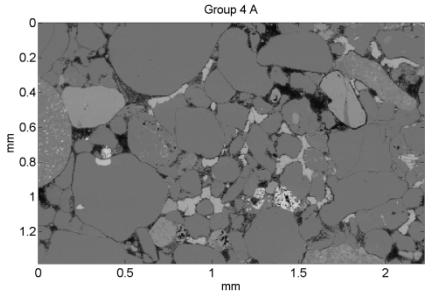
Group 4 A
mm
mm

p

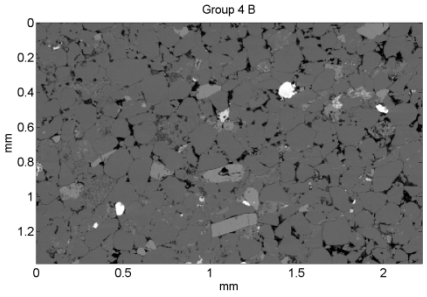
Group 4 B
mm
mm

q

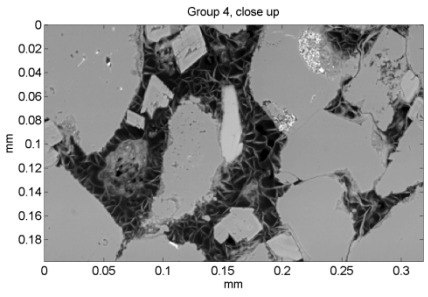
Group 4, close up
mm
mm

r

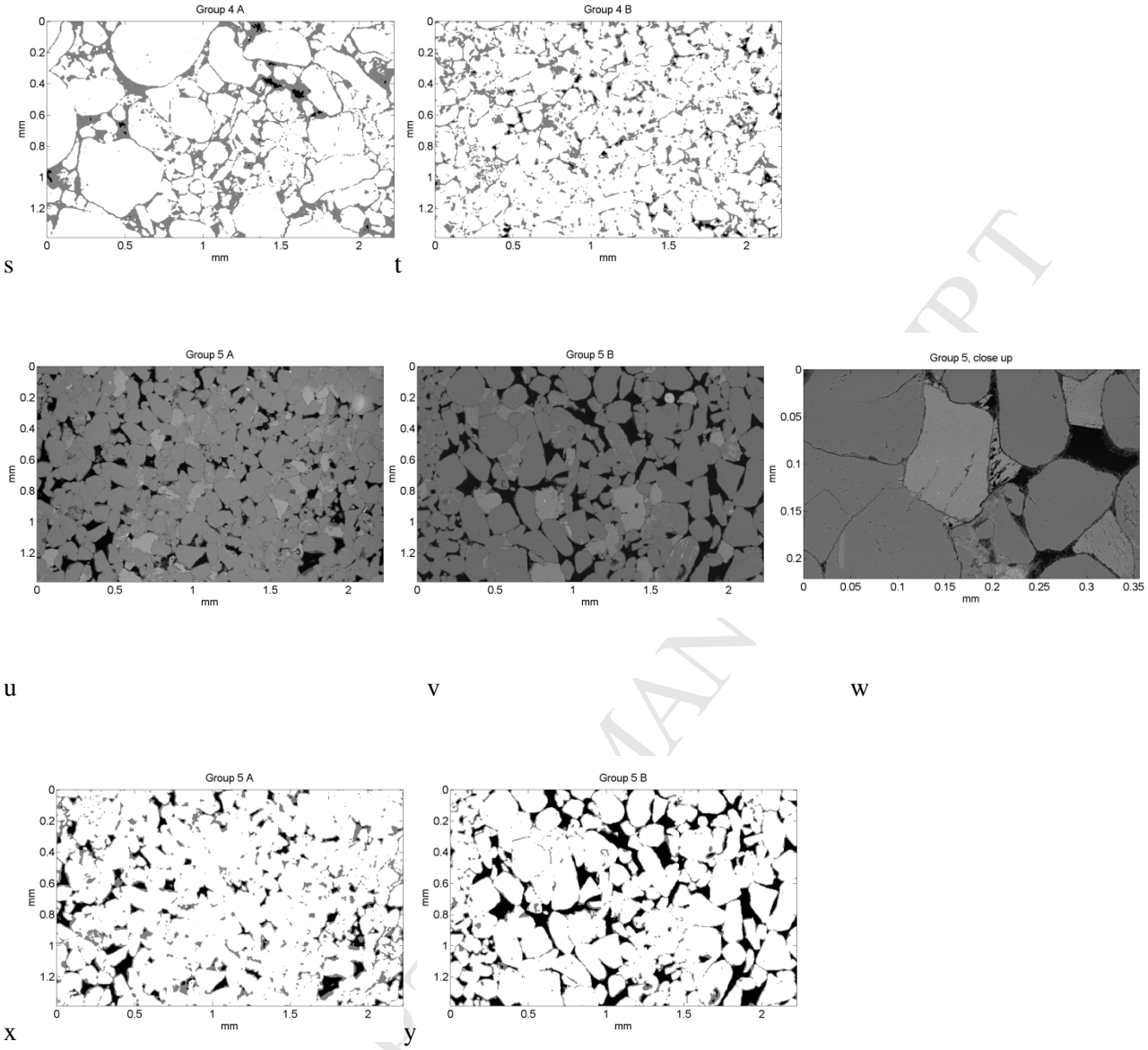

Figure 2: Representative backscatter electron microscopy (BSEM) images for a sample with a lower mean NMR T_2 (samples A) and a sample with a higher mean T_2 (samples B) from each of the five groups. Below BSEM images are processed images where white pixels are grains, grey pixels contain clay minerals and porosity and black pixels are clay-free porosity. Pixel length of images used for image analysis is 3 μm/pixel, and for close up images 0.6μm/pixel. Orientation unknown.

Table 2: Image analysis with a resolution of 3 μm/pixel was used to quantify the area fractions. Error margins in brackets on image analysis data are based on the maximum difference among two or three images

of the same sample. Clay mineral volume per sample from XRD is calculated by taking porosity and mineral density into account (Durand et al., 2000; Grim, 1953).

			Experimental		Images	
		Nr of samples with similar NMR T_2 distribution	He-porosity (m^3/m^3) %[a]	Clay (XRD) (m^3/m^3) %	Clay all pores (m^2/m^2) %	Clay-free pores (m^2/m^2) %
Gr 1	A	7	12.2	16 (3)	32 (3)	1.0 (0.2)
	B	2	19.5	12 (2)	37 (2)	2.5 (0.4)
Gr 2	A	5	10.3	13 (3)	19 (1.1)	1.4 (0.3)
	B	6	11.1	11 (3)	17 (1.0)	4.2 (1.1)
Gr 3	A	8	9.2	11 (2)	20 (0.8)	0.3 (0.5)
	B	6	17.5	12 (3)	31 (2)	4.1 (0.7)
Gr 4	A	4	9.2	4.5 (1)	17 (3)	0.49 (0.04)
	B	16	10.6	5.1 (1)	19 (3)	1.17 (0.11)
Gr 5	A	3	16.4	7.0 (2)	19 (0.9)	4.6 (0.3)
	B	4	17.9	6.6 (2)	23 (0.9)	13.2 (0.9)

4.2.2 NMR and mercury injection porosimetry

Figure 3 shows the NMR curves and the differential Hg saturation curves. To compare the logarithmically spaced NMR data to mercury data, the pore diameters on mercury injection are equally spaced on the logarithmic axis (Lenormand, 2003).

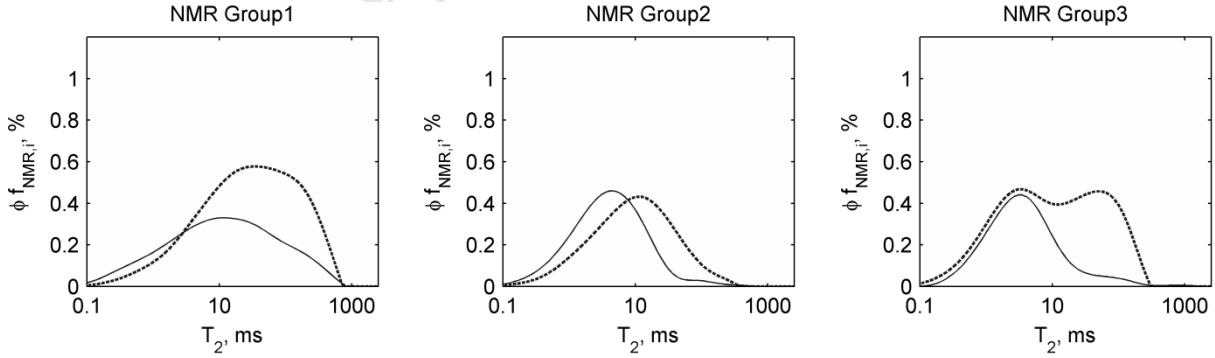

a b c

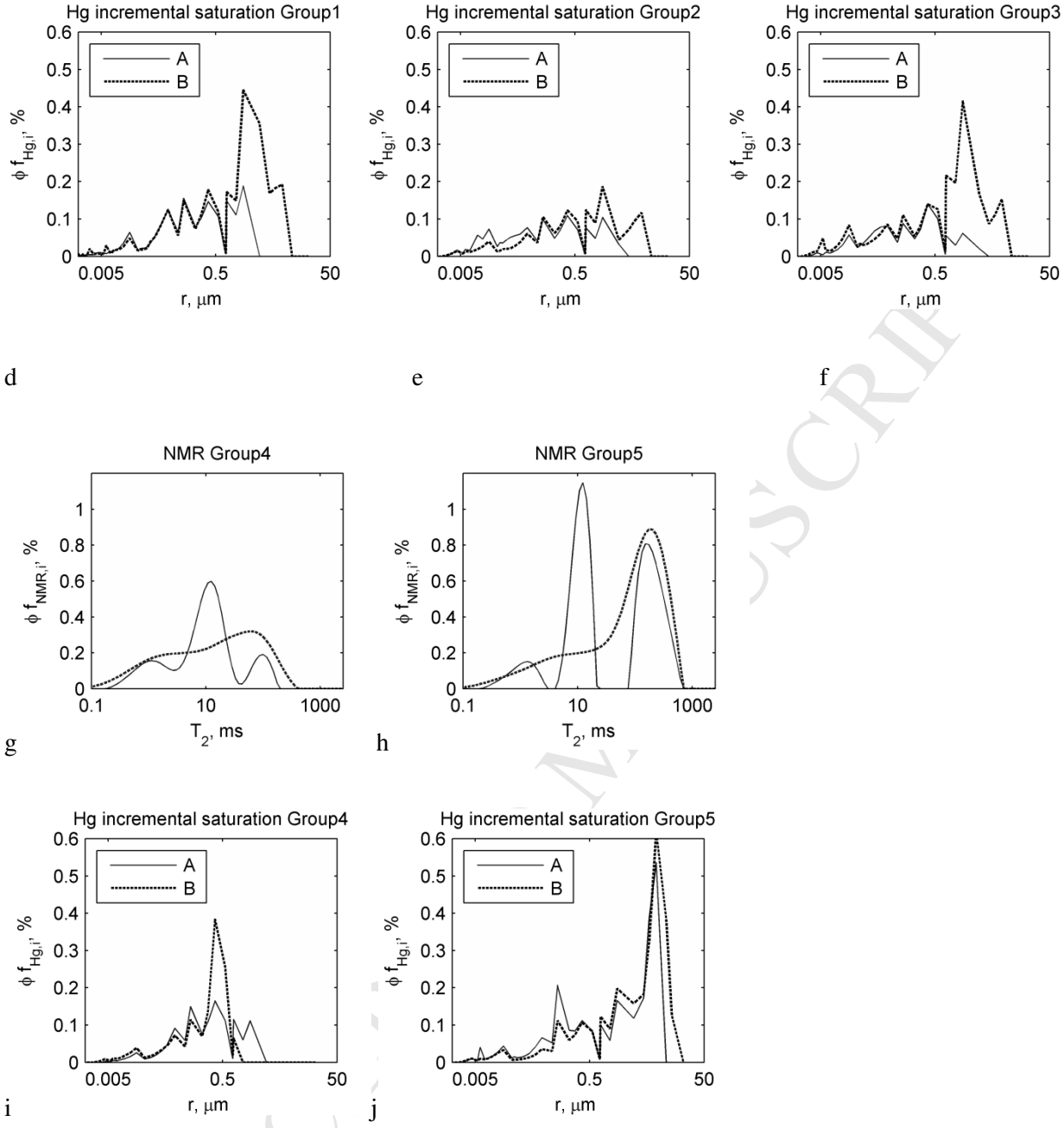

Figure 3: Differential NMR T_2-plots and radii obtained from incremental mercury injection (Hg) using the Washburn equation for representative samples with a lower mean T_2 (samples A) and a higher mean T_2 (samples B). The fraction of the porosity, f_i that corresponds to a given T_{2i} or r_i is multiplied by the sample porosity in order to show differences among the total porosity of the samples as well as their pore size distribution. (The legend in the mercury plots also applies to the NMR plots.)

4.3 Permeability

Figure 4a shows that scatter in the permeability-porosity trend is largest in groups 3 and 5 and least in groups 1 and 4. The relation between porosity and the ratio of gas permeability to brine permeability likewise shows scatter (Figure 4b). Samples with a higher permeability in Group 5 represent intervals with a low illite content. Samples in Group 1 with a high porosity have low carbonate content, however, due to the high kaolinite and illite contents, these samples have a relatively low permeability.

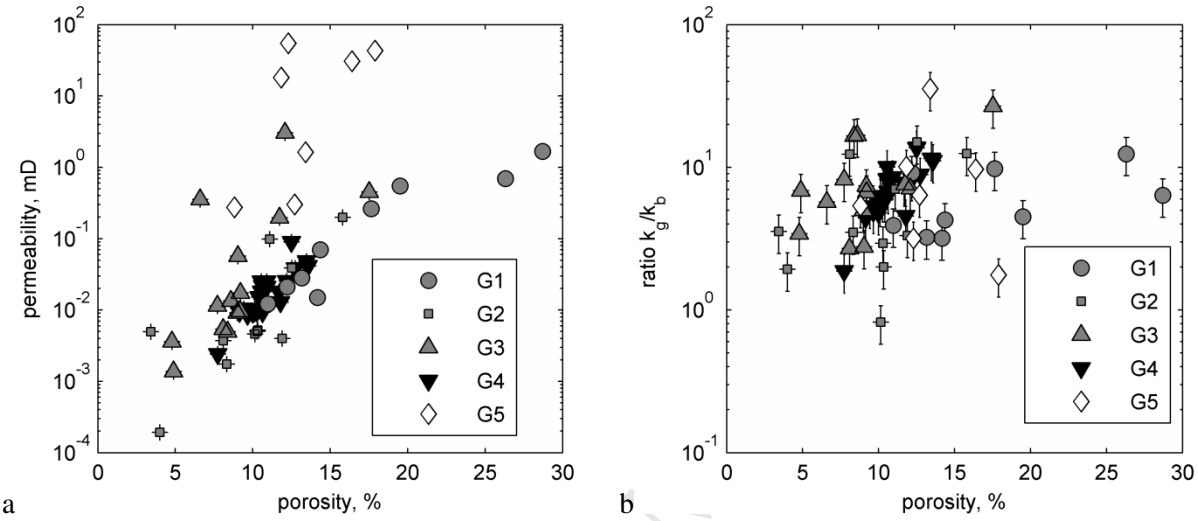

Figure 4: a) Porosity and gas permeability, k_g, at in situ confining stress for 63 samples divided into five subgroups based on mineralogy. b) The ratio of gas permeability to brine permeability, k_b, ranges between 1 and 30 and shows no correlation with porosity.

5. Discussion

5.1 Mineralogy and pore space

The NMR curves cannot directly be related to the texture that is observed in images. Samples can have similar NMR curves but a different distribution of clay minerals in the pore space, e.g. samples 2A and 3A (Figure 3b, 3c), where the former sample contains grain lining illite/mica (Figure 2f, 2h, 2i), whereas the latter sample contains illite fibres and kaolinite platelets filling pore bodies (Figure 2k, 2m, 2n). Also, samples that have similar pore size can have different NMR curves, e.g. samples 5A and 5B which have only

a limited amount of grain lining illite/mica and similar Hg-curves, yet the NMR curves are different (Figure 2u, 2v, 2x, 2y, 3h, 3j).The mineralogy and abundance of clay minerals as determined from XRD were observed to reflect sandstone texture as observed in BSEM images, so therefore samples are grouped based on clay mineralogy.

In Group 1 sandstones kaolin platelets are distributed throughout the pore space, and there is little clay-free porosity in the segmented images (Figure 2d and e; Table 2). These samples have a single broad T_2 peak, which indicates a continuous range of pore sizes (Figure 3a). As compared to sample 1A, sample 1B has more clay-free porosity in images, and accordingly the modes of both the NMR and the Hg data correspond to a larger equivalent pore size.

In Group 2 illite/mica and chlorite platelets line the grain surface (Figure 2f-h). We observed both clay platelets in random orientation to the grains and a thin layer of clay minerals parallel to the grain surface (Figure 2h). Other authors have also observed sheets of illite parallel to the grain surface, from which thin illite laths or fibres protrude into the pore space (Desbois et al., 2011; Wilson and Pittman, 1977). This morphology of illite, forming sheets that extend into laths was also observed in SEM and BSEM images of Group 3 (Figure 2m, 5).

The mode of the NMR curves of samples 2A and 2B is smaller than the mode of samples 1A, 1B, 4A and 4B; whereas the mode of the Hg-curves is higher in Group 2 samples than in the Group 2 and Group 4 samples (Figure 3). The difference might be due to the fibrous illite in Group 2, which may collapse on the grain surface during drying (Luffel et al., 1993), or deform during the Hg-injection. This would result in a larger equivalent pore size from Hg injection data than from NMR-testing of these samples.

A larger pore size for Hg-injection than for NMR is also observed in the samples from Group 3. Scanning electron microscopy (SEM) images of dried samples show illite protruding into the pore volume and illite fibres that might have collapsed during drying (Figure 5). The Hg-curve for sample 3B shows only one peak at large pore sizes, as opposed to the two approximately equal peaks in NMR (Figure 3c and f). The lack of a peak for smaller pore sizes in the Hg-curve could be due to deformation of illite, and in principle also be due

to incomplete mercury saturation. However with a maximum capillary pressure of 413.7 MPa, the minimum accessible pore size would be 2 nm cf. Eq.2.

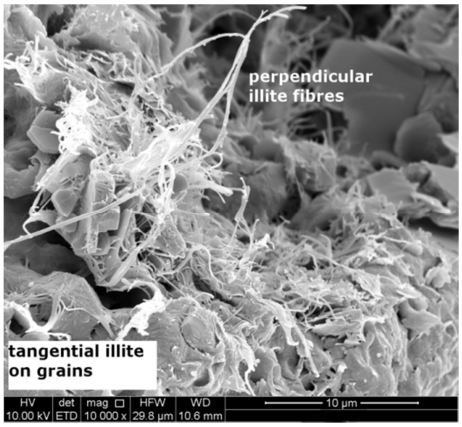

Figure 5: Scanning electron microscopy (SEM) image of illite in sample 3B. Dense tangential mats of illite can be seen on the grain surface as well as illite fibres that protrude into the pore space perpendicular to grains.

Group 4 samples contain illite/mica particles, which are mainly observed as thin fibres that bridge the pores (Figure 2r). This results in a small clay-free pore area, despite the relatively low clay mineral content (Figure 2s and t; Table 2). The NMR curve (Figure 2g) of sample 4A shows distinct peaks, indicating a discontinuous pore size distribution, which could be related to poor sorting (Figure 2p). The maximum pore size would be expected to reflect pores among the clay particles, as there is little clay-free porosity (Figure 2s and 2t). The maximum pore sizes from mercury injection are 1.5 µm and 0.8 µm in samples 4A and 4B respectively (Figure 3i), which is in the same order of size as the pores in fibrous illite observed by Desbois et al. (2011) in high resolution focussed ion beam scanning electron microscopy (FIB-SEM) images of Rotliegend gas sandstone. Whereas the maximum T_2 in sample 4B is larger than in sample 4A, the maximum equivalent pore size on the Hg-curve is higher in sample 4A. This might be due to the 'ink-bottle' effect: when mercury enters larger pores through connecting smaller pores, the size of the larger pores is not reflected in the Hg-curve.

In Group 5 only a very thin layer of chlorite or illite fibres that are perpendicular to the grain surface is observed (Figure 2w). Whereas samples in Group 4 have a similar clay content per pore volume, clay minerals bridge the pores in those samples, which results in a lower clay-free porosity than in Group 5 samples (Table 2). Whereas the Hg-curves of samples 5A and 5B have a similar shape, the NMR curves have different shapes (Figure 3h 3j). The prominent peak for smaller T_2 that is observed in NMR for sample 5A is missing in the Hg-curve. This might be due to incomplete Hg saturation or alteration of the clay morphology during sample drying, or be due to deformation of illite during Hg-injection.

5.2 Surface relaxivity from NMR and Hg-injection

In order to relate T_2 time to equivalent pore size or S_p the value of ρ is required. Surface relaxivity was estimated from surface area per bulk volume, S, from Hg-injection and S from NMR. Groups 1, 2 and 5 have a mean ρ of 8-9 μm/s; groups 3 and 4 have mean ρ of 12-13 μm/s. For the entire dataset ρ = 10 μm/s with standard deviation 4 μm/s.

The surface relaxivity of quartz (99.5% SiO_2) and kaolin samples (purity 99.9%) measured using high salinity NaCl solution are only 3.6 μm/s and 3.9 μm/s respectively (Alam et al., 2014). Those authors calculated relaxivity in tests with distilled water, NaCl, $CaCl_2$, $MgCl_2$ and Na_2SO_4 solutions with different salinities. Relaxivity varies between 2.9 μm/s – 3.9 μm/s for quartz and 1.1 μm/s - 5.0 μm/s for kaolin, however, no consistent trend with ion type or salinity was observed. The higher relaxivities estimated may be due to the presence of iron-bearing minerals in the sandstone samples.

Iron bearing minerals, such as siderite, chlorite, or hematite, can increase the surface relaxivity (Keating and Knight, 2007, 2010; Matteson and Tomanic, 2000). Keating and Knight (2010) measured ρ exceeding 19 μm/s for mixtures of quartz and siderite with an iron content of 0.6 wt.%, and they found that ρ increases with increasing iron content. Keating and Knight (2007) showed that quartz sand coated with hematite has ρ greater than 18 μm/s, whereas sand coated with goethite with the same iron content has ρ of only 1.6 μm/s, indicating that the structural relation in which iron is present affects ρ. All 63 samples contain Fe-dolomite, and additionally samples in groups 2 and 5 contain chlorite, and samples in groups 3 and 5 contain siderite.

Figure 6 shows no correlation between the content of iron bearing minerals from XRD and ρ, presumably because the effect of iron on ρ depends on the type of iron bearing minerals.

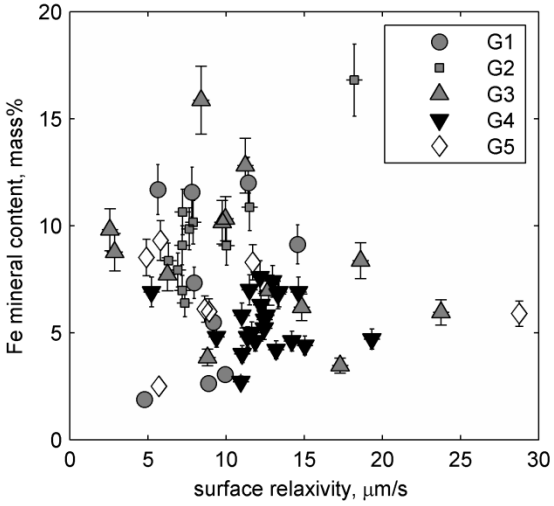

Figure 6: The iron bearing mineral content (dolomite, siderite, pyrite and chlorite) from X-ray diffraction (XRD) and surface relaxivity as calculated from Hg-injection data.

Differences among ρ for different groups could also be due to the experimental methods. Hg-injection reflects the size of pore throats through which pore bodies, are accessed, whereas NMR reflects the pore bodies (Coates et al., 1999; Dastidar et al., 2006). Incomplete mercury saturation would yield a higher ρ. Some authors match the modes for the differential Hg-curve and the differential NMR curve to estimate ρ, (Coates et al., 1999; Dastidar et al., 2006). For samples in Group 5, this results in ρ ranging from 1 μm/s to 300 μm/s, as opposed to 5 μm/s to 12 μm/s. The large range, and the outliers where ρ exceeds values reported by Keating and Knight (2007, 2010) suggest that ρ estimated from the modes of the curves are more sensitive to experimental artefacts than ρ estimated from S. Presumably because connectivity among pore bodies primarily affect larger pores, whereas S in Eq. 4 is controlled by smaller pores. Other authors match the cumulative curves (Mbia et al., 2014). For samples whose NMR and Hg- curves have different shapes,

e.g., 1B, 4A, 3B, and 5A, only a segment of the total curves overlaps for a given ρ. When ρ is chosen so that the curves overlap for the smallest pores, the results are comparable to ρ calculated from S.

5.3 Permeability modelling

Permeability is modelled per pore size increment from NMR cf. Eq. 12. As differences in the surface relaxivity among samples could be due to experimental artefacts, the average and standard deviation of ρ for the dataset, 10 µm/s ± 4 µm/s, are used.

The permeability per T_2 increment (Eq. 12), and the cumulative sum of permeability are shown for samples 1A and 5B in Figure 7a and 7b. Permeability per increment increases steeply with increasing T_2, therefore the contribution of the smallest pores to the cumulative permeability is negligible. However, the cumulative permeability in sample 1A is three orders of magnitude higher than the measured permeability: 21 mD as opposed to 0.021 mD. Even the permeability in the individual increments with a T_2 > 20 ms exceeds the measured permeability (Figure 7c).This indicates that the larger pores do not form a percolating flow path.

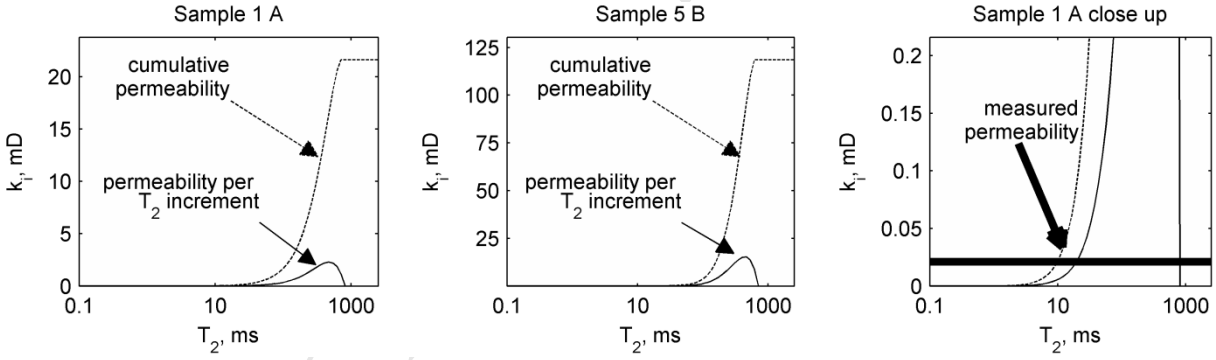

a b c

Figure 7: The permeability for each increment of the porosity distribution k_i and the cumulative permeability are shown for sample 1A (a) and sample 5b (b). For sample 1A the measured permeability is significantly lower than the permeability in the larger pores; the cumulative permeability is three orders of magnitude higher than the measured permeability (c). For sample 5B cumulative permeability is of the same order of magnitude as the measured permeability (Figure 8c) (Surface relaxivity is 10 µm/s).

When smaller pores, with a high S_p and a low permeability, limit flow through larger pores, the sample permeability would not reflect the size of the larger pores. Therefore we do the opposite of what is done in general practice and define a cut-off T_2, $T_{2,i_{max}}$ where the cumulative permeability equals the measured permeability. The fraction of the porosity in the pores up to $T_{2,i_{max}}$ is then considered effective to permeability. and this fraction $f_{\phi,eff}$ will be given by:

$$f_{\phi,eff} = \sum_{i=1}^{i_{\max}} f_{NMR,i}$$

Eq. 20

Within the fraction of pores that is effective to permeability the largest pores make the largest contribution to the measured permeability, due to the steep increase in permeability with increasing T_2. Figure 8 shows the cumulative permeability up to the cut-off for representative samples with different NMR curves. Sample 1A represents samples that have a broad single peak in the NMR curve. The cut-off T_2 approximately coincides with the mode of the T_2 distribution, which also coincides with the geometrical mean T_2, $T_{2,Gmean}$. Sample 4A represents samples with multiple peaks where pores with $T_2 < T_{2,Gmean}$ control permeability, whereas sample 5B represents samples where larger pores with $T_2 > T_{2,Gmean}$ also contribute to permeability. The shape of the curve does not indicate the fraction of pores contributing to permeability, e.g., for Sample 5A with a shape similar to Sample 4A larger pores do contribute to permeability.

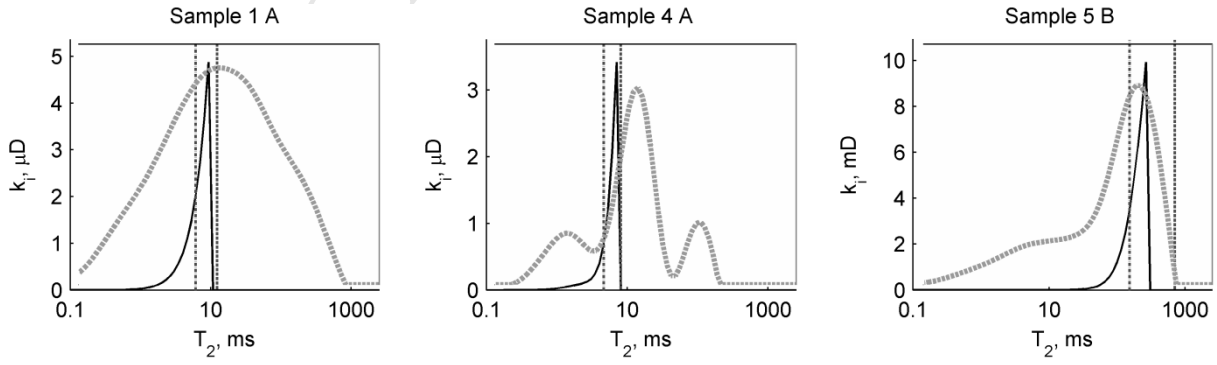

a b c

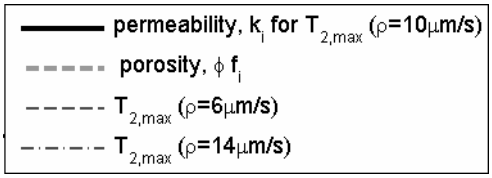

Figure 8: The permeability for each segment of the porosity distribution k_i is shown for the pores that dominate permeability by assuming surface relaxivity ρ =10μm/s. To achieve the measured permeability only a part of the porosity is required. This is 50%, 40% and 90% of the total porosity in samples 1A, 4A and 5B respectively. The full pore size distribution, $\phi\ f_i$ is shown by the dashed grey line; vertical dashed black lines indicate the cut-off T_2, $T_{2,max}$ when permeability is modelled using $\rho = 6$ μm/s and $\rho = 14$ μm/s.

Connectivity cannot be directly measured from 2D images; however, the fraction of clay-free porosity indicates in which samples clay-free pores are connected, and the clay-free porosity exceeds 2 % for samples where $T_{2,max} > T_{2Gmean}$ (1B, 2B, 3B, 5A, 5B, Table 2). This is in the same order as percolation porosity values for clay-free sandstones found by Mavko and Nur (1997) and by Walderhaug et al. (2012). In clay-free samples below the percolation threshold, intergranular pores might only be connected by microcracks. Similarly, in clay-rich samples where the clay-free porosity is below a threshold, the intergranular pores might only be connected by pores among clay minerals.

Microcracks along grain boundaries and through clay particle aggregates are observed in images, these could affect permeability. Accordingly permeability measurements with a lower confining stress show a higher permeability in these samples. Therefore, permeability was measured at in situ stress levels, to minimise the effect of microcracks. As a first approximation, flow in microcracks is not included in the permeability modelling.

The fraction of the clay-free porosity does however not predict $f_{\phi,eff}$, e.g., Samples 5A and 5B have the same $f_{\phi,eff}$, although sample 5B has a three times higher clay-free porosity (Tables 2 and 3). The extent to which larger pores contribute to flow would depend on the pore shape and 3D connectivity, which is not characterised by only clay-free porosity. The image resolution and thresholds would also affect quantification of clay-free porosity. Nonetheless, for a comparison among a set of sandstones using the same

images, image segmentation, rather than the shape of the NMR curve or the clay content from XRD, gave the best prediction of samples in which permeability would be controlled by smaller pores.

Table 3: Effective fraction of porosity is the fraction of porosity that accounts for the measured permeability. The maximum effective pore radius corresponds to maximum T_2 of the effective fraction of porosity, and effective specific surface $S_{p,eff}$ is calculated from the measured permeability and the total effective porosity. Immobile layer thickness is the thickness of bound water that would result in the measured brine permeability if the maximum effective pore radius to brine flow were the same as to gas flow. Refer to text for details. Error margins in brackets indicate result range for ρ 6-14 μm/s.

Group		Measured Permeability mD	Effective fraction of porosity	Maximum effective radius to gas μm rho=10μm/s	$S_{p,eff}$ m^2/cm^3 rho=10μm/s	Immobile layer thickness nm
1	A	0.021	0.49 (0.07)	0.20 (0.02)	23 (2)	40 (10)
	B	0.55	0.55 (0.09)	0.70 (0.04)	6.1 (0.5)	120 (30)
2	A	0.0052	0.55 (0.11)	0.09 (0.02)	45 (5)	10 (2)
	B	0.099	0.68 (0.12)	0.35 (0.05)	12.0 (1.1)	100 (20)
3	A	0.0096	0.70 (0.12)	0.11 (0.03)	35 (3)	22 (4)
	B	0.45	0.76 (0.08)	0.81 (0.07)	7.6 (0.4)	210 (20)
4	A	0.0094	0.40 (0.10)	0.15 (0.03)	27 (4)	35 (5)
	B	0.022	0.46 (0.07)	0.231 (0.010)	20 (2)	45 (5)
5	A	31	0.87 (0.11)	5.0 (0.3)	0.96 (0.06)	1100 (100)
	B	43	0.87 (0.14)	5.7 (0.7)	0.85 (0.07)	550 (50)

When permeability is controlled by a fraction of the pore volume, the specific surface that is effective with regards to permeability would be the specific surface relative to the fraction of pores that control permeability. The mean effective specific surface, $S_{p,eff}$, was calculated from the effective porosity and permeability:

$$S_{p,eff} = \sqrt{\frac{c\phi f_{\phi_{eff}}}{k}}$$

Eq. 21

Figure 9 shows $S_{p,eff}$ as a function of volumetric clay content per intergranular volume (porosity + clay mineral volume). Samples in different groups fall on different trends. As $S_{p,eff}$ characterises the specific surface that controls permeability, samples with different clay mineralogy would fall on different trends when micropores among clay minerals control permeability. Accordingly, samples dominated by illite fibres, which have a high specific surface, in Group 4 have the highest $S_{p,eff}$ for a given clay content; samples containing kaolin or mica/illite platelets with a lower specific surface (Group 1 and 3) show a lower $S_{p,eff}$. In samples from Group 5 intergranular pores appear to control permeability; therefore these have the lowest $S_{p,eff}$ reflecting the larger intergranular pores.

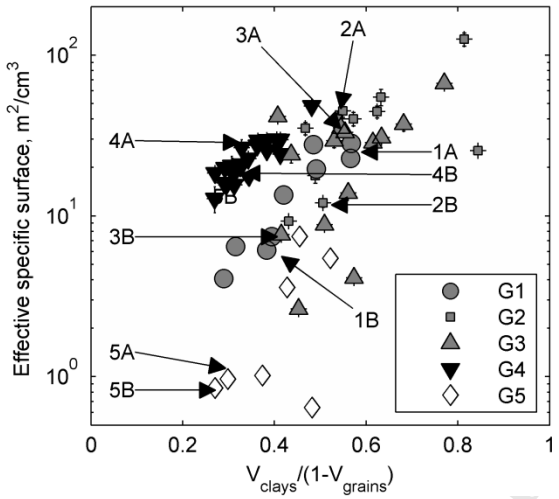

Figure 9: Effective specific surface area versus clay volume scaled by intergranular volume $(V_{clay})/(1 - V_{grains})$. Samples from different groups have different clay types and different clay morphologies. This results in a different effective specific surface area for a given clay content.

5.3.1 Permeability modelling: gas slip

As a first approximation to characterize the effect of gas slip on our results we used the mean effective radius r_{eff} in Eq. 14. In these tests with a pore pressure of 6.7 MPa, $\lambda \approx 3$ nm for helium (Eq. 15). The effect of gas slip cf. Eq. 13and Eq. 14 would be largest for sample 2A, which has the smallest r_{eff} (Table 3); in this

sample k_a/k = 1.3. The summation of k_i up to the lower true permeability k yields r_{max} = 0.076 ± 0.007 μm as compared to the r_{max} = 0.087 ± 0.008 μm for the measured permeability and $f_{\phi,eff}$ = 0.51 ± 0.11 as compared to 0.55 ± 0.11. The difference due to slip is smaller than the difference due to the error margin on ρ. For the other samples that have a larger r_{eff} the effect of gas slip would be even smaller.

5.3.2 Permeability modelling: immobile water

The measured brine permeability is lower than the measured gas permeability for all samples (Figure 4b). On average gas permeability is eight times higher than brine permeability; which is significantly larger than the effect of gas slip estimated in Section 4.4. One reason for the difference in permeability to brine and water could be a layer of bound water on the mineral surface that reduces the pore volume that is available to brine flow (Andreassen and Fabricius, 2010; Heid et al., 1950; Luffel et al., 1993; Solymar et al., 2003). Another reason could be the reversible collapse of fibrous illite during drying (De Waal et al., 1988; Luffel et al., 1993).

To model the permeability in the presence of a layer of immobile water, we assumed that the same size pores are effective for flow of gas and brine. Therefore, from summation of $k_{w,i}$ (cf. Eq. 19) up to the same cut-off $T_{2,i}$ that was obtained from gas permeability and the measured brine permeability we estimated the value of τ that would be required to account for the measured permeability difference between gas and brine. Figure 10 shows the gas and the brine porosity and permeability distributions for representative samples.

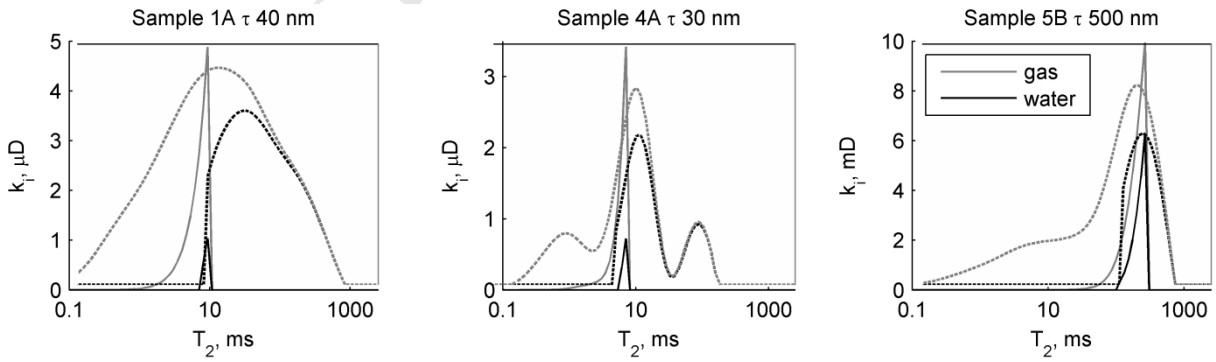

a b c

Figure 10: The permeability k_i is shown up to the maximum T_2, $T_{2,max}$, where the cumulative k_i equals the measured permeability for gas. Brine permeability is shown for the immobile layer thickness, τ, which accounts for the measured water permeability. The porosity to brine is lower than the porosity to gas due to the immobile water on the pore walls.

For samples in groups 1, 3 and 4, τ is in the order of 50 nm, whereas for samples in Group 5, τ ranges up to 1 μm (Fig. 11). Measurements of the bound water layer are affected by the experimental techniques used (Goertz et al., 2007), however, experiments with flow through thin quartz capillaries indicate a bound water layer thickness of 8 nm (Zheleznyi et al., 1972). Other authors have suggested even lower values, in a range of 0.5-4 nm (Grim, 1953; Khilar and Fogler, 1984).The higher estimated τ suggests that other factors contribute to the lower brine permeability.

Fines mobilisation might occur when the EDL repulsion between fines and the pores walls is high (Khilar and Fogler, 1984). During flow with concentrated (>5000 ppm) NaCl solution, Khilar and Fogler (1984) observed no mobilisation; the permeability was only reduced when the salinity fell below 4000 ppm. Therefore, we would not expect fines migration with the 200,000 ppm NaCl solution that was used in the current tests. Precipitation of salts might alter the pore geometry, however, no precipitates were observed in BSEM images.

Alteration or collapse of fibrous illite clay mineral as suggested by Luffel et al. (1993) could account for the observed differences between gas and brine permeability. Those authors observed a five times higher permeability to gas than to brine in a sample with 0.7 mD permeability; they report that the effect of drying was larger in samples with a lower permeability. All groups contain 5% illite or more, and clay fibres perpendicular to the grain surface can be observed in BSEM and SEM images (Figures 3 and 5). The presence of illite perpendicular to the grains in Figure 5 indicates that not all illite fibres collapsed during

drying, which was also observed in North Sea samples by Wilson et al. (2014).

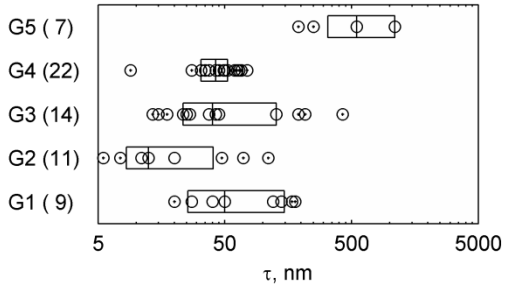

Figure 11: The thickness of bound water, τ, that would need to be invoked in order to account for the measured difference between gas and brine permeability if the same pores controlled flow. The mobile porosity to brine may be lower than to gas due to a combination of bound water on the mineral surface and to illite fibres that are perpendicular to the grain surface in a saturated sample but collapse on the grain surface during drying.

6. Conclusions

We analysed permeability to brine and to gas for 63 Rotliegend sandstone samples by means of nuclear magnetic resonance transverse relaxivity data, mercury injection, X-ray diffraction, and image analysis.

- Permeability to gas was modelled using the pore size distribution from NMR to estimate which pores control flow. In samples with a low clay-free porosity, larger pores do not form a connected flow path and permeability is controlled by the smaller pores. In 38 out of 63 samples the measured gas permeability could be accounted for by the fraction of porosity with a pore size smaller than the mean pore size.
- Permeability to brine was modelled by taking a supposed immobile water layer into account; however, in several samples a bound water layer greater than 100 nm was required to account for measured brine permeability. This indicates that other factors, such as the presence of fibrous illite also contribute to the lower brine permeability.

- Surface relaxivity was estimated from the specific surface area as calculated from mercury injection data and the specific surface area from NMR data. The average surface relaxivity for 63 samples was 10 µm/s.

9. Acknowledgements

We acknowledge Aurelian, BG, BP, EBN, Shell and Wintershall. Rosenbrand acknowledges funding from the Otto Mønsted fund and the Danish Council for Strategic Research. We thank two anonymous reviewers for a comprehensive review and constructive feedback.

References

Alam, M. M., Katika, K., Fabricius, I. L., 2014. Effect of salinity and specific ions on amount of bound water on quartz, calcite and kaolinite, as observed by NMR transverse relaxation time (T2). In 76th EAGE Conference and Exhibition. Amsterdam RAI, The Netherlands: Amsterdam RAI, The Netherlands

Andreassen, K., Fabricius, I. L., 2010. Biot critical frequency applied to description of failure and yield of highly porous chalk with different pore fluids. GEOPHYSICS. 75, E205–E213

API, 1998. Recommended Practices for Core Analysis, API RP 40. Washington: American Petroleum Institute: Washington

Berryman, J.G., Blair, S.C., 1987. Kozeny–Carman relations and image processing methods for estimating Darcy's constant. J. Appl. Phys. 62, 2221–2228

Brower, K.R., Morrow, N.R., 1985. Fluid Flow in Cracks as Related to Low-Permeability Gas Sands. SPEJ 25, 191–201

Byerlee, J., 1990. Friction, overpressure and fault normal compression. Geophys. Res. Lett. 17, 2109–2112

Carman, 1937. Fluid flow through granular beds. Trans. Instn Chem. Engrs. 15, 150-166

Cornell, D., Katz, D.L., 1953. Flow of Gases through Consolidated Porous Media. Ind. Eng. Chem. 45, 2145–2152

Cao, B., Sun, J., Chen, M., Guo, Z., 2009. Molecular Momentum Transport at Fluid-Solid Interfaces in MEMS/NEMS: A Review. Int. J. Mol. Sci. 10, 4638–4706

Coates, G. R., Xiao, L., Prammer, M. G., 1999. NMR Logging Principles and Applications. Houston: Halliburton Energy Services: Houston

Dullien, F.A.., 1975. Invited Review Single Phase Flow Through Porous Media and Pore Structure. Chem. Eng. J. 10, 1–34

Dastidar, R., Sondergeld, C. H., Rai, C. S., 2006. NMR Desaturation and Surface Relaxivity Measurements on Clastics Rocks. In SPE EUROPEC/EAGE Annual Conference and Exhibition. Vienna, Austria

De Waal, J. A., Bil, K. J., Kantorowicz, J. D., Dicker, A. I. M., 1988. Petrophysical Core Analysis Of Sandstones Containing Delicate Illite. Log Anal. Sept-Oct, 317–331

Desbois, G., Urai, J. L., Kukla, P. A., Konstanty, J., Baerle, C., 2011. High-resolution 3D fabric and porosity model in a tight gas sandstone reservoir: A new approach to investigate microstructures from mm- to nm-scale combining argon beam cross-sectioning and SEM imaging. J. Pet. Sci. Eng. 78, 243–257

Durand, C., Cerepi, A., Brosse, E., 2000. Effect of pore-lining chlorite on petrophysical properties of low-resistivity sandstone reservoir. In Proceedings - SPE Annual Technical Conference and Exhibition.

Gaupp, R., Okkerman, J. A., 2011. Diagenesis and reservoir quality of Rotliegend sandstones in the Northern Netherlands - A review. Soc. Sediment. Geol. SEPM Spec. Publ. 98, 193–226

Giesche, H., 2006. Mercury porosimetry: a general (practical) overview. Part. Part. Syst. Charact. 23, 9–19

Goertz, M. P., Houston, J. E., Zhu, X.-Y., 2007. Hydrophilicity and the viscosity of interfacial water. Langmuir. 23, 5491–5497

Grim, R. E., 1953. Clay Mineralogy. (Vol. 1). New York: McGraw-Hill Book Company inc.: New York, 384 pp

Heid, J. G., McMahon, J. J., Nielsen, R. F., Yuster, S. T., 1950. Study of the Permeability of Rocks to Homogeneous Fluids. In Drilling and Production Practice, 230-246.

Hillier, S., 1999. Use of an air brush to spray dry samples for X-ray powder diffraction. Clay Miner. 34, 127–135

Hillier, S., 2000. Accurate quantitative analysis of clay and other minerals in sandstones by XRD: comparison of a Rietveld and a reference intensity ratio (RIR) method and the importance of sample preparation. Clay Miner. 35, 291–302

Hossain, Z., Grattoni, C. A., Solymar, M., Fabricius, I. L., 2011. Petrophysical properties of greensand as predicted from NMR measurements. Pet. Geosci. 17, 111–125

Hunt, A.G.., 2009. Percolation theory for flow in porous media. Springer, 319 pp

Jones, F. O., Owens, W. W., 1980. A Laboratory Study of Low-Permeability Gas Sands. SPE J. Pet. Technol. 32, 193–199

Jones, S. C., 1997. A Technique for Faster Pulse-Decay Permeability Measurements in Tight Rocks. SPE Form. Eval. 12, 19–26

Keating, K., Knight, R., 2007. A laboratory study to determine the effect of iron oxides on proton NMR measurements. Geophysics. 72, E27–E32

Keating, K., Knight, R., 2010. A laboratory study of the effect of Fe (II)-bearing minerals on nuclear magnetic resonance (NMR) relaxation measurements. Geophysics. 75, F71–F82

Khilar, K., Fogler, H., 1984. The existence of a critical salt concentration for particle release. J. Colloid Interface Sci. 101, 214-224

Kozeny, J., 1927. Über kapillare Leitung des Wassers im Boden. Sitzungsberichte Der Akad. Der Wissenschaften Wien, Math. Klasse. 136, 271–306

Landrot, G., Ajo-Franklin, J. B., Yang, L., Cabrini, S., Steefel, C. I., 2012. Measurement of accessible reactive surface area in a sandstone, with application to CO2 mineralization. Chem. Geol. 318-319, 113–125

Lenormand, R., 2003. Interpretation of mercury injection curves to derive pore size distribution. In International Symposium of the Society of Core Analysts. Pau France

Luffel, D., Herrington, K., Walls, J., 1993. Effect of Drying on Travis Peak Cores Containing Fibrous Illite. SPE Adv. Technol. Ser. 1, 188–194

Lyklema, J., de Keizer, A., Bijsterbosch, B., Fleer, G.J., Cohen Stuart, M.A., 1995m Fundamentals of Interface and Colloid Science. Volume 2, Chapter 3, Elsevier B.V. 232 pp.

Matteson, A., Tomanic, J., 2000. NMR relaxation of clay/brine mixtures. SPE Reserv. Eval. Eng. 3, 408–413

Mavko, G., Nur, A., 1997. The effect of a percolation threshold in the Kozeny-Carman relation. Geophysics. 5, 1480–1482

Mbia, E. N., Fabricius, I. L., Krogsbøll, A., Frykman, P., Dalhoff, F., 2014. Permeability, compressibility and porosity of Jurassic shale from the Norwegian-Danish Basin. J. Pet. Geosci. (In press)

McBride, E. F., 1963. A classification of common sandstones. J. Sediment. Res. 33, 664–669

Mortensen, J., Engstrøm, F., Lind, I. ., 1998. The Relation Among Porosity, Permeability, and Specific Surface of Chalk From the Gorm Field, Danish North Sea. SPE Reserv. Eval. Eng. 1, 245–251

Ostensen, W.R., 1983. Microcrack Permeability in Tight Gas Sandstone. Soc. Pet. Eng. J. 23, 919–927

Pape, H., Tillich, J.E., Holz, M., 2006. Pore geometry of sandstone derived from pulsed field gradient NMR. J. Appl. Geophys. 58, 232–252

Peters, C. A., 2009. Accessibilities of reactive minerals in consolidated sedimentary rock: An imaging study of three sandstones. Chem. Geol. 265, 198–208

Rootare, H. M., Prenzlow, C. F., 1967. Surface areas from mercury porosimeter measurements. J. Phys. Chem. 71, 2733–2736

Solymar, M., Fabricius, I. L., Middleton, M., 2003. Flow characterization of glauconitic sandstones by integrated Dynamic Neutron Radiography and image analysis of backscattered electron micrographs. Pet. Geosci. 9, 175–183

Torrent, J., Schwertmann, U., 1987. Influence of hematite on the color of red beds. J. Sediment. Petrol. 57, 682–686

Walderhaug, O., Eliassen, a., Aase, N. E., 2012. Prediction of Permeability In Quartz-Rich Sandstones: Examples from the Norwegian Continental Shelf and the Fontainebleau Sandstone. J. Sediment. Res. 82, 899–912

Walsh, J.B., Brace, W.F., 1984. The effect of pressure on porosity and the transport properties of rock. J. Geophys. Res. Solid Earth 89, 9425–9431

Washburn, E. W., 1921. The Dynamics of Capillary Flow. Phys. Rev. 17, 273

Wilson, M. D., Pittman, E. D., 1977. Authigenic clays in sandstones; recognition and influence on reservoir properties and paleoenvironmental analysis. J. Sediment. Res. 47, 3–31

Wilson, L., Wilson, M. J., Green, J., Patey, I., 2014. The Influence of Clay Mineralogy on Formation Damage in North Sea Reservoir Sandstones: A Review with Illustrative Examples. Earth-Science Rev. (accepted manuscript)

Zheleznyi, B. V, Zorin, Z. M., Sobolev, W. D., Churaev, N. V, 1972. Experimental study of properties of water in thin films and fine capillaries. Bull. Int. Assoc. Eng. Geol. 5, 57–61

Highlights

- Permeability of 63 Rotliegend sandstone samples is analysed.
- Permeability is modelled using pore size distributions from NMR.
- Surface relaxivity is estimated from NMR and Hg injection.
- Brine permeabilities are modelled by estimating a bound water layer.
- The presence of illite clays may contribute to a lower brine permeability.